Circularly-Polarized Fabry-Perot Antenna Using a Hybrid Leaky-Wave Mode

Antoine Calleau, Maria Garcia-Vigueras, Hervé Legay, Ronan Sauleau, Mauro Ettorre

Circularly-Polarized Fabry-Perot Antenna Using a Hybrid Leaky-Wave Mode

Antoine Calleau, María García-Vigueras, *Senior Member, IEEE*, Hervé Legay, Ronan Sauleau, *Fellow, IEEE* and Mauro Ettorre, *Senior Member, IEEE*

Abstract—A spectral Green's function approach is developed here to analyze Fabry-Perot antennas for the generation of circular polarization. The structure consists of a single cavity, created between a partially reflective surface and a high impedance surface, fed by a low directive linearly polarized source. The elements in the antenna are characterized by tensor impedances. This frame allows to conceive a circularly polarized antenna supporting a single hybrid leaky-wave mode. By means of a residue analysis, it is demonstrated that the use of a single hybrid leaky mode is sufficient to generate circular polarization. The tool is validated by an antenna design matched over a relative bandwidth of 28.5% with an axial ratio lower than 3 dB.

Index Terms—Fabry-Perot antennas, leaky-wave antennas, circular polarization, spectral Green's functions

I. Introduction

FABRY-PEROT antennas (FPAs) have been extensively researched for the past decades for their capability of creating a large radiating aperture while keeping the antenna simple and compact [1]. The original concept consists of a cavity created between a partially reflective surface (PRS) and a ground plane excited by a low directive source [1]. Since their introduction, FPAs have considerably evolved and numerous implementations can be found in literature showing gain enhancement capability [2], [3], beam steering [4], beam shaping [5]–[7], or even radar cross section reduction [8]. The ground plane may be replaced by a high impedance surface (HIS) to allow sidelobes reduction [9], profile reduction [10], [11], or higher control of the beam steering [12], [13] for instance. In many applications that consider space to earth links or multi-path media, circular polarization (CP) is required. CP-FPAs have been broadly studied for the past decade, and diverse contributions can be found in literature. Three general strategies can be identified to generate CP. In the first strategy the cavity is fed by a CP primary source that can be either a patch [14], [15], a sequentially rotated slot array [16], or even an array of patches [17]. The use of such CP sources often implies bulky and complex feeding networks and the use of dielectric materials. A second strategy consists in considering a linearly polarized (LP) primary source. It can be either a vertical [18] or a horizontal source slanted

A. Calleau, M. Ettorre and R. Sauleau are with the Institute of Electronics and Telecommunications of Rennes (IETR), UMR CNRS 6164, University of Rennes 1, 35042 Rennes, France (e-mail: antoine.calleau@univ-rennes1.fr).

M. G. Vigueras is with the Institute of Electronics and Telecommunications of Rennes (IETR), UMR CNRS 6164, Rennes Institut of Applied Sciences, 35042 Rennes, France.

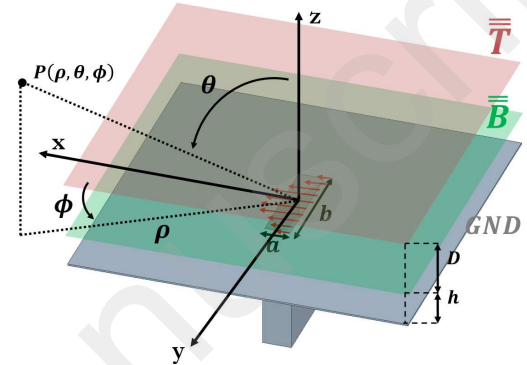H. Legay is with the Research and Development Department, Thales Alenia Space, 31037 Toulouse, France.

Fig. 1. View of the Fabry-Perot antenna under study, where the top partially reflective and the bottom high impedance surfaces are characterized by infinite tensor impedances T and B, respectively. (ρ, θ, ϕ) are the cylindrical coordinates.

by $45°$ in the azimuthal plane [19]–[24]. The latter launches both a Transverse Electric (TE) and a Transverse Magnetic (TM) mode within the cavity [25] interacting with the different elements of the antenna to create CP. The present manuscript is based on a third strategy that consists of a self-polarizing cavity. This method was firstly introduced in [26] and it is here considered from a different perspective.

In the cited references of the previous paragraph, various analysis frames are proposed, with different levels of accuracy. As in [19]–[21], [23], [24], [26], the antenna is seen as a resonator where the wave number is assumed to be $\beta = k_0$ (k_0, the free space wave-number) and the field is solved using a ray tracing method. A more accurate method that considers the complex nature of the wave number can be found in [22], [27]. However, in the two aforementioned references, the source (a coaxial probe, or a patch antenna) is not described in the analysis and it is assumed to be a point source.

In the present manuscript, an analytical approach to characterize accurately FPAs with arbitrary tensorial sheet impedances in the stack-up and considering the effect of the feeding source is proposed. The tool is used to analyze CP-FPAs, with broadside radiation, fed by a linearly polarized (LP) source parallel to the ground plane. It allows to analyze such antennas from a leaky-wave (LW) perspective. It results that CP can be theoretically produced by the proposed FPA by the excitation of a single hybrid leaky-wave (HLW) mode within the cavity. As a result, the HLW is here used to create CP and at the same time enhances the directivity of the elementary source. The proposed approach eases the design
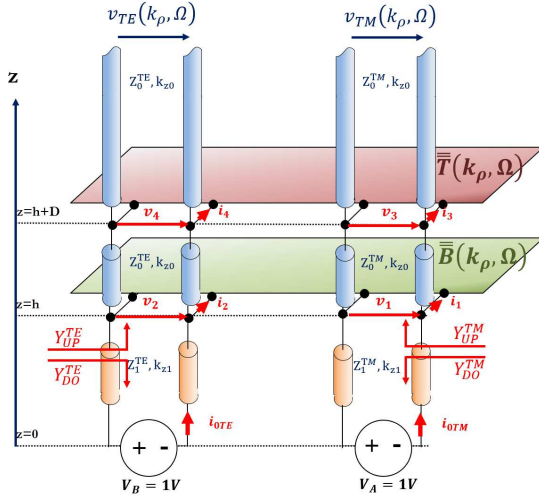
Fig. 2. Equivalent T-Line Network of the structure in Fig. 1.

of the antenna by using ideal tensorial sheet impedances for the stack-up of the cavity. The required impedance boundaries are then synthesized by using the full-wave commercial solver ANSYS HFSS. The paper is organized as follows. In section II, the spectral GFs analysis of the proposed antenna is developed. In section III, design guidelines are provided based on the performance analysis of possible antenna configurations. Some assumptions are made for the formulation. They are clearly identified and justified, and their limits of validity discussed. Section IV is dedicated to the synthesis of a single-mode CP-FPA. A layout for the PRS and the HIS is obtained. Full-wave results validate the proposed approach and main conclusions. The performance of the antenna is then compared to the state of the art. Finally, conclusions are drawn in section V.

II. SPECTRAL GREEN'S FUNCTION FPA ANALYSIS

The structure under study is presented in Fig. 1. It consists of a single FP cavity created between a tensorial PRS ($\overline{\overline{T}}$) on the top, and a tensorial HIS ($\overline{\overline{B}}$) over a ground plane. Free space is assumed between the different layers, however other materials may be considered without affecting the formulation. The cavity is fed by one or several LP apertures with size $a \times b$ placed in the ground plane. Such apertures are fed by a monomodal rectangular waveguide with the electric field polarized along x.

Resorting to a spectral GF analysis, the structure presented in Fig. 1 can be equivalently represented by the transmission-line network sketched in Fig. 2, where the two transmission-lines account for both TE and TM modal solutions. Their corresponding modal impedances are $Z_0^{TE} = \xi k_0/k_{z0}$ and $Z_0^{TM} = \xi k_{z0}/k_0$ where $k_{z0} = \sqrt{k_0^2 - k_\rho^2}$ is the wave number along z axis, $k_\rho = \sqrt{k_y^2 + k_x^2}$, and ξ is the free-space impedance. For the sake of completeness, and in order to consider any possible case where coupling could exist between TE and TM modes, the impedances $\overline{\overline{T}}$, and $\overline{\overline{B}}$ are represented as tensors (their definitions are given in Appendix

TABLE I
DESIGN CONFIGURATIONS.

	Capacitive-Inductive	Inductive	Capacitive
h (mm)	5	5	2.5
D (mm)	8.1	5.2	6
T_{22} (Ohm)	-j9000	-j9000	-j9000
T_{11} (Ohm)	j130	j200	j200
T_{12} (Ohm)	0	0	0
B_{22} (Ohm)	-j30	j420	-j275
B_{11} (Ohm)	j100	j950	-j675
B_{12} (Ohm)	j110	j500	j500

A). Considering the general case for which T_{12}, T_{21}, B_{12}, B_{21} are non-zero and using the superposition theorem [28], the voltages v_{TM} and v_{TE} at the end of the lines presented in Fig. 2 can be defined as:

$$v_{TM/TE}(k_\rho, \Omega) = v_{3/4}(k_\rho, \Omega, z) = \begin{cases} v_{3/4}^{v_A}(k_\rho, \Omega, z) \\ \quad or \\ v_{3/4}^{v_B}(k_\rho, \Omega, z) \end{cases}, \quad (1)$$

with $k_\rho = \sqrt{k_x^2 + k_y^2}$ and $\Omega = tan(k_y/k_x)$. The details of the calculations are given in Appendix B. As presented in Fig.2, the v_A (v_B) superscript refers to the case where a voltage source is placed in the TM (TE) line and the one in the TE (TM) line is replaced by a short-circuit. Following [28], chapter 12.9.3, the total far field can be evaluated for each ϕ cut-plane, yielding:

$$\begin{bmatrix} E_\theta(\theta, \phi) \\ E_\phi(\theta, \phi) \end{bmatrix} = j\frac{k_0 e^{-jk_0 r}}{2\pi r} \times \begin{bmatrix} 1 \\ cos(\theta) \end{bmatrix} \times$$

$$\tilde{\boldsymbol{G}}_t^{EM}(k_\rho, \Omega, v_{TE}, v_{TM})\tilde{\boldsymbol{M}}_t(k_\rho, \Omega), \quad (2)$$

where $k_\rho = k_0 sin(\theta)$, and $\Omega = \phi$. In (2), $\tilde{\boldsymbol{M}}_t(k_\rho, \Omega)$ is the Fourier transform of the magnetic current distribution at $z = 0$. $\tilde{\boldsymbol{G}}_t^{EM}(k_\rho, \Omega, v_{TE}, v_{TM})$ is the spectral dyadic Green's function [29], its definition is given in Appendix C. The EM superscript indicates that G_t^{EM} is associated to the electric field due to a magnetic current distribution.

III. DISPERSION ANALYSIS

A. Uniform impedance sheets

The natural resonances of the antenna stack-up can also be derived. Let us first consider that $\overline{\overline{T}}$ and $\overline{\overline{B}}$ are uniform. Therefore, no coupling exists between TE and TM modes and $\overline{\overline{T}}$ and $\overline{\overline{B}}$ are diagonal matrices of the form

$$\overline{\overline{T}}(k_\rho, \Omega) = \begin{bmatrix} T & 0 \\ 0 & T \end{bmatrix}, \overline{\overline{B}}(k_\rho, \Omega) = \begin{bmatrix} B & 0 \\ 0 & B \end{bmatrix}. \quad (3)$$

By looking at Fig. 2, two Transverse Resonant Equations (TREs) [30] can be defined in the considered scenario by considering the TE and TM transmission lines in Fig. 2:

$$Y_{UP}^{TE/TM}(k_{\rho,sol}^{TE/TM}, f) + Y_{DO}^{TE/TM}(k_{\rho,sol}^{TE/TM}, f) = 0, \quad (4)$$

As it is well known, the solutions of a TRE (values of $k_{\rho,sol}^{\text{TE/TM}}$) define the modal solutions satisfying the boundary conditions of the structure [30]. Leaky-wave modes supported by the structure are therefore characterized by a $k_{\rho,sol}^{TE/TM}$ that is complex and that varies with the frequency [31]

$$k_{\rho,sol}^{\text{TE/TM}}(f) = \beta_{sol}^{\text{TE/TM}}(f) - j\alpha_{sol}^{\text{TE/TM}}(f). \quad (5)$$

In (5), $\beta_{sol}^{\text{TE/TM}}$ is the phase constant and $\alpha_{sol}^{\text{TE/TM}}$ the leakage rate, both associated to the leaky-wave modal solution. Since no coupling is considered between the TE and TM modes, the TE and TM lines in Fig. 2 are uncoupled, and several leaky-wave modes may be supported by the cavity. These solutions have naturally different dispersive behavior.

B. Diagonal tensorial impedance sheets

Let consider $\overline{\overline{B}}$ and $\overline{\overline{T}}$ of the form

$$\overline{\overline{B}}(k_\rho, \Omega) = \left[R^{-1}(\Omega)\right] \begin{bmatrix} B_{11}(0) & 0 \\ 0 & B_{22}(0) \end{bmatrix} \left[R(\Omega)\right], \quad (6)$$

$$\overline{\overline{T}}(k_\rho, \Omega) = \left[R^{-1}(\Omega)\right] \begin{bmatrix} T_{11}(0) & 0 \\ 0 & T_{22}(0) \end{bmatrix} \left[R(\Omega)\right], \quad (7)$$

where $B_{11} \not\equiv B_{22}$, $T_{11} \not\equiv T_{22}$, and $R(\Omega)$ is defined in (23). In that case, as presented in [32], TE and TM modes are uncoupled in the principal planes $\phi = 0°$ and $\phi = 90°$, and the dispersion equations are the one in (4). In all the other planes, $\overline{\overline{B}}$ and $\overline{\overline{T}}$ are not diagonal and TE and TM modes couple, pertaining to hybrid modes. Therefore, equations (4) become rigorously equivalent. As a consequence, pairs of hybrid leaky-wave (HLW) modes may exist in the cavity as the two TREs in (4) become identical and equal to:

$$Y_{UP}^{hyb}(k_{\rho,sol}^{hyb}, \Omega, f) + Y_{DO}^{hyb}(k_{\rho,sol}^{hyb}, \Omega, f) = 0, \quad (8)$$

where the superscript *hyb* indicates that the solutions are consistent to hybrid modes. The propagation constant associated to the hybrid leaky-wave modes depends on the observation plane, due the anisotropy of the PRS and the HIS.

C. Non-diagonal tensorial impedance sheets

Let's consider now that $\overline{\overline{B}}$ and $\overline{\overline{T}}$ are of the form

$$\overline{\overline{B}}(k_\rho, \Omega) = \left[R^{-1}(\Omega)\right] \begin{bmatrix} B_{11}(0) & B_{12}(0) \\ B_{21}(0) & B_{22}(0) \end{bmatrix} \left[R(\Omega)\right], \quad (9)$$

$$\overline{\overline{T}}(k_\rho, \Omega) = \left[R^{-1}(\Omega)\right] \begin{bmatrix} T_{11}(0) & 0 \\ 0 & T_{22}(0) \end{bmatrix} \left[R(\Omega)\right]. \quad (10)$$

As discussed in [32], since $\overline{\overline{B}}(k_\rho, 0)$ is non-diagonal, an angle $\Omega\prime \neq n\pi/2$ with $n \in \mathbb{Z}$ exists so that $\overline{\overline{B}}(k_\rho, \Omega\prime)$ is a diagonal matrix. However, since $\overline{\overline{T}}(k_\rho, 0)$ is diagonal, $\overline{\overline{T}}(k_\rho, \Omega\prime)$ is a non-diagonal tensor. As a consequence, for any azimuthal plane ϕ, coupling exists between TE and TM modes and the dispersion equation corresponds to equation (8). As demonstrated in Section IV, such a mode will be used to create CP.

IV. DESIGN GUIDELINES FOR CP-FPA

In this section, guidelines are provided to design CP-FPA, supporting a single HLW mode radiating broadside with the intention of identifying the most promising scenarios. The goal is to assess the configuration maximizing the axial ratio bandwidth (AR-BW) [28] of the antenna.

A. Single-mode operation

As illustrated in Fig. 1, the considered primary source is polarized along x. To avoid higher-order mode excitation and for manufacturing issues, both h and D are fixed around quarter wavelength at the operating frequency. The tensor impedance considered for the PRS is of the type (11) corresponding to a classical case considered in literature [26] for which the PRS only interacts with the x-polarized field while being transparent to y-polarized waves. The PRS is assumed loss less and purely reactive around the operating frequency, therefore it can be written as:

$$\overline{\overline{T}}(k_\rho, \Omega) = \left[R^{-1}(\Omega)\right] \begin{bmatrix} T_{11} & 0 \\ 0 & -j\infty \end{bmatrix} \left[R(\Omega)\right], \quad (11)$$

where T_{11} is purely imaginary. By inspecting (11) it can be deduced that the PRS is inductive or capacitive when T_{11} is positive or negative. The reflectivity of the PRS depends solely on the magnitude of T_{11}. Higher value of T_{11} corresponds to a more transparent PRS.

Since $\overline{\overline{B}}$ is a tensorial impedance of the form (9), coupling between TE and TM modes is introduced and only hybrid leaky-wave modes are supported by the cavity, as demonstrated in Section III.C . Considering that the source is polarized along x, a single hybrid mode is excited, generating a CP field. This avoids the need for equal dispersive behavior for both TE and TM solutions to assure CP [18]. The HIS and the PRS should be tuned appropriately to generate CP, thus determining the remaining unknowns T_{11}, B_{11}, B_{22}, and B_{12}. In the following, the polarization operation is attributed to the HIS while the gain enhancement is attributed to the PRS [22].

B. Design of the HIS

Assuming T_{11} is fixed, $\overline{\overline{B}}$ must be chosen by looking to the axial ratio (AR) performance. The latter will be tuned to target CP at broadside. Figure 3 presents the variation of the AR for a fixed value of T_{11}. By tuning B_{12}, an infinite number of potential solutions can be theoretically found. Those solutions can be divided into three groups. One for which both B_{11} and B_{22} are positive (inductive case), a second one for which both B_{11} and B_{22} are negative (capacitive case) and a third one for which the impedance have opposite signs (capacitive-inductive case). For the sake of completeness, and to benchmark the performance of the different solutions, three different antennas with directivity around 13 dBi at 15 GHz are synthesized, their characteristics are given in Table I.

The impedances are assumed to be independent of the frequency as well as the incidence in the elevation plane and an analysis of the behavior of the three designs is carried
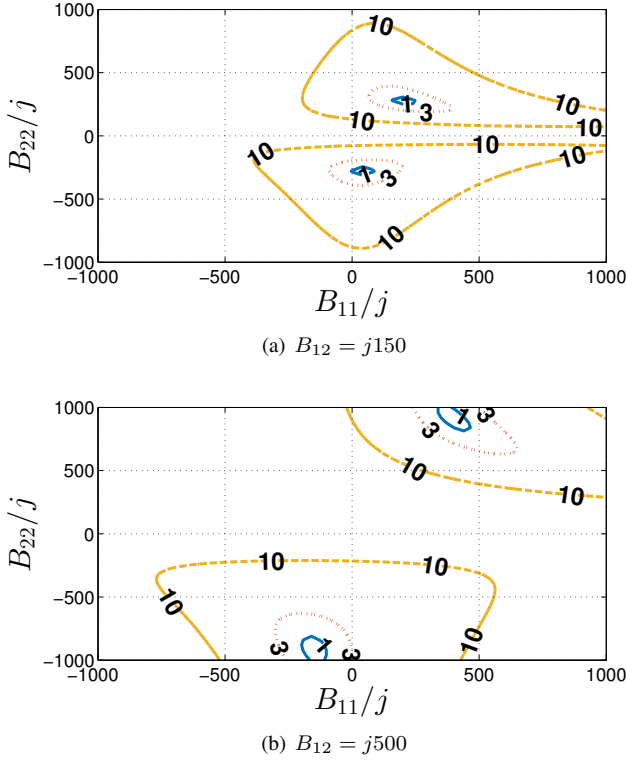
(a) $B_{12} = j150$

(b) $B_{12} = j500$

Fig. 3. Contour plots of the AR at 15GHz with respect to B_{11} and B_{22} for different values of B_{12}. $h = 5mm$, $D = 5.5mm$, $T_{11} = j200$ Ohm, and $T_{22} = -j1.3.10^4$ Ohm.

(a)

(b)
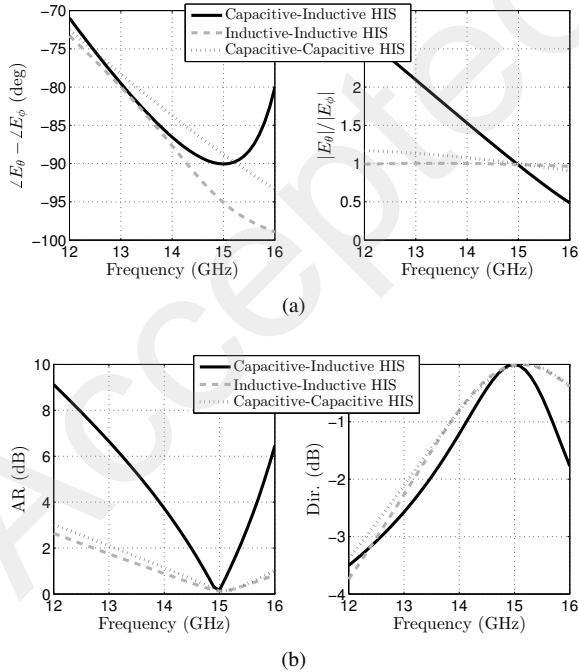
Fig. 4. Broadside radiation: (a) phase difference between E_ϕ and E_θ (left), magnitude ratio between E_ϕ and E_θ (right), and (b) Axial Ratio over the frequency (left) and directivity (right).
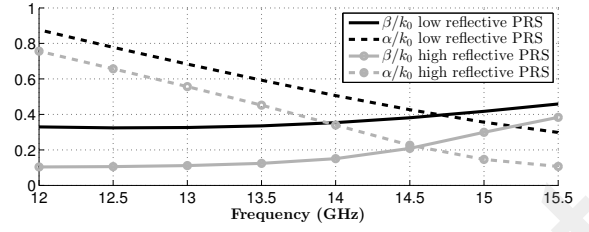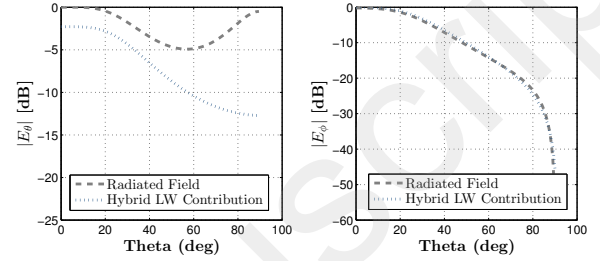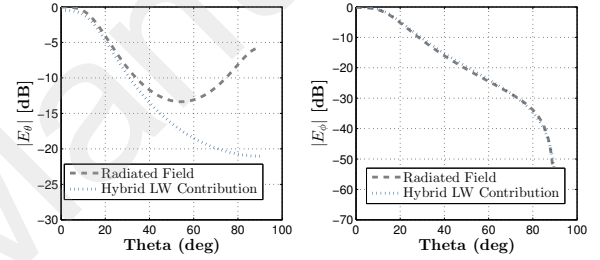

Fig. 5. Dispersion diagram of the designs presented in Table I

(a) Low reflective PRS : $T_{11} = j200$, $B_{11} = j950$, $B_{22} = j420$

(b) High reflective PRS : $T_{11} = j100$, $B_{11} = j1860$, $B_{22} = j200$

Fig. 6. Radiation patterns of the LW contribution and the total field for both E_θ and E_ϕ components along the plane $\phi = 0$. $h = 5$ mm, $D = 5.2$ mm, and $B_{12} = j500$.

out. Directivity and AR comparisons are proposed in Fig. 4 (b). The three cases show similar directivity behavior but the capacitive-inductive design can be discarded when comparing the axial ratio bandwidth (AR-BW). Indeed, although the phase difference between E_ϕ and E_θ presented in Fig. 4(a) (left) presents similar variations, the variations of the magnitude ratio between the two components (Fig. 4(a) (right)) for the capacitive-inductive case are much stronger that the ones for the capacitive or the inductive cases. Regarding the AR-BW, the capacitive and the inductive cases are therefore the most promising solutions.

Considering the proximity between the HIS and the ground plane for the capacitive configuration (see Table I) and the manufacturing issues linked to it, the inductive design is chosen. An inductive surface can be easily synthesized with a mesh of metallic strips [33], [34]. The synthesis is proposed in the next section.

C. Design of the PRS and impact on the LW radiation

In this section, we highlight the fact that although both the leaky modal solutions of the cavity and the direct radiation from the primary source contribute to the radiated fields,
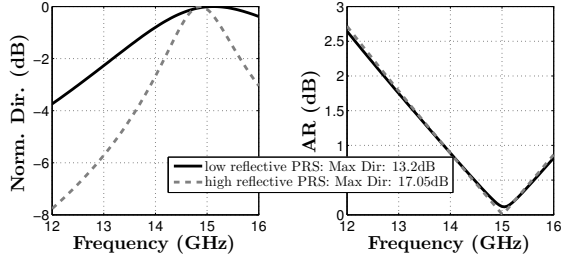
Fig. 7. Normalized field pattern (left) and AR (right) of the designs presented in Fig. 6

the HLW generates the component necessary to create CP. In the following we intend to assess the impact of the LW contribution to the total radiated field, and thus, the fact that the LW could be the only responsible for the generation of CP (since direct radiation from the source is LP). Following [31], [35] the contribution of the LW to the radiated field can be approximated by the following residue analysis

$$
\begin{bmatrix} E_\theta^{hlw}(\theta,\phi) \\ E_\phi^{hlw}(\theta,\phi) \end{bmatrix} \approx j \frac{k_0 e^{-jk_0 r}}{2\pi r} \frac{2k_{\rho,sol}^{hyb}(k_\rho,\Omega)}{k_\rho^2 - k_{\rho,sol}^{hyb^2}(k_\rho,\Omega)} \times
$$
$$
\mathcal{R}es\left[\tilde{\boldsymbol{G}}_t^{EM}(k_\rho,\Omega,v_{TE},v_{TM})\tilde{\boldsymbol{M}}(k_\rho,\Omega), k_{\rho,sol}^{hyb}(k_\rho,\Omega)\right],
$$
(12)

where $k_\rho = k_0 sin(\theta)$, and $\Omega = \phi$. $\mathcal{R}es(\tilde{\boldsymbol{G}}_t^{EM}(k_\rho,\Omega,v_{TE},v_{TM})\tilde{\boldsymbol{M}}(k_\rho,\Omega), k_{\rho,sol}(k_\rho,\Omega))$ is the residue of $\tilde{\boldsymbol{G}}_t^{EM}(k_\rho,\Omega,v_{TE},v_{TM})\tilde{\boldsymbol{M}}(k_\rho,\Omega)$ at $k_{\rho,sol}^{hyb}$. The superscript *hlw* indicates that the field is the one radiated by the HLW. In order to illustrate the contribution of the LW to the CP radiated far field, two examples are next analyzed where $T_{11} = j100$ Ohm or $j200$ Ohm thus implying high/low PRS reflectivity cases. The dispersion of the two aforementioned cases is presented in Fig. 5. As expected, the leakage rate of the high reflectivity case is much lower than the one of the low reflectivity case. Figure 6 presents the comparison between the magnitude of the field radiated by the LW, evaluated with (12), and the total field, evaluated with (2), for both E_θ and E_ϕ, in the plane $\phi = 0$. By looking at the E_ϕ component, it can be noticed that this component of the radiated fields is only created by the LW. In Fig. 7 the normalized directivity and the AR of both designs are presented. Thanks to the single HLW in the cavity, it is demonstrated that the AR bandwidth is independent of the directivity peak. Consequently, the technique is particularly interesting for small apertures, for which the gain bandwidth is large. Therefore, it can be deduced that the HLW not only is responsible for the gain enhancement of the cavity but also for the generation of CP over a wide band. Although the gain enhancement is highly related to the leakage rate, and so to the PRS reflectivity, in the following T_{11} is fixed to $j200$ Ohm to get wide 3dB directivity BW.
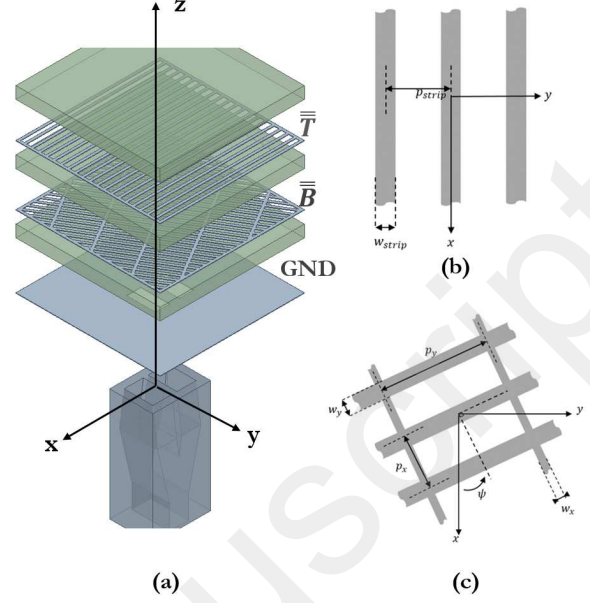

Fig. 8. Fabry-Perot antenna under study. $D = 5.2$ mm, $h = 5$ mm. For manufacturing simplicity: $w_{strip} = 1$ mm, and $p_{strip} = 7$ mm. Therefore, to realize the chosen impedances: $w_x = 0.5$ mm, $w_y = 4$ mm, $p_x = 10.6$ mm, $p_y = 12.3$ mm and $\psi = 59°$. The slots size are $a = 8$ mm, $b = 12$ mm and are separated by a distance $sep = 2$ mm. Rohacell HF51 foam is considered between the elements.

V. ANTENNA SYNTHESIS

A. Design Procedure

When synthesizing the desired values of the impedances, it is desirable to opt for low dispersive and non-resonating cell topologies. Both the PRS and HIS geometries in Fig. 8 are chosen to provide a constant behavior with the frequency around the frequency of operation and with respect to angles of incidence close to broadside. This assumption is in line with the analytical approach proposed in the previous sections. As presented in [37], the reflection properties of a surface impedance can be determined by its Floquet's harmonics scattering matrix such as:

$$
\Gamma^{\overline{\overline{T}}/\overline{\overline{B}}}(k_\rho,\Omega) = \begin{bmatrix} \Gamma_{11}^{\overline{\overline{T}}/\overline{\overline{B}}}(k_\rho,\Omega) & \Gamma_{12}^{\overline{\overline{T}}/\overline{\overline{B}}}(k_\rho,\Omega) \\ \Gamma_{21}^{\overline{\overline{T}}/\overline{\overline{B}}}(k_\rho,\Omega) & \Gamma_{22}^{\overline{\overline{T}}/\overline{\overline{B}}}(k_\rho,\Omega) \end{bmatrix}.
$$
(13)

To synthesize the antenna, the topologies depicted in Fig. 8 have been chosen for the PRS and HIS. The PRS is made out of periodic metallic strips aligned with x in order to provide a $\overline{\overline{T}}$ matrix of the type (11). The width of each strip is w_{strip} and the period is p_{strip}. If $w_{strip} \sim \lambda/10$, and $w_{strip}\backslash p_{strip} \ll 1$, the strip grid can be considered as transparent for the y-polarization [38] and the assumption made in (11) remains valid. For the case of the HIS, both the phase of $\Gamma_{11}^{\overline{\overline{T}}}(k_\rho,0)$

TABLE II

Reference	Source Polarization	Max. directivity	-10dB-S_{11} BW	3dB-directivity BW	3dB-AR BW
[24]	LP	10 dBi	2.6 %	>5 %	**0.85** %
[20]	LP	13.5 dBi	10 %	>10 %	**1.9** %
[23]	LP	12.4 dBi	3.7 %	7.9 %	**6** %
[36]	CP	12 dBi	13.9 %	19 %	**13** %
This work	LP	13.2 dBi	23.5 %	21.5 %	**28.5** %

and $\Gamma_{22}^{\overline{\overline{T}}}(k_\rho, 0)$ can be written

$$\Gamma_{11}^{\overline{\overline{T}}}(k_\rho, 0) = \frac{\overline{\overline{T}}_{11}(k_\rho, 0) - Z_0^{TM}(k_\rho, 0)}{\overline{\overline{T}}_{11}(k_\rho, 0) + Z_0^{TM}(k_\rho, 0)}$$

$$\Gamma_{22}^{\overline{\overline{T}}}(k_\rho, 0) = \frac{\overline{\overline{T}}_{22}(k_\rho, 0) - Z_0^{TE}(k_\rho, 0)}{\overline{\overline{T}}_{22}(k_\rho, 0) + Z_0^{TE}(k_\rho, 0)}, \qquad (14)$$

they both vary less than 5% over the frequency band.

The HIS is a mesh of inductive strips of widths w_x and w_y with periodicity p_x and p_y rotated by an angle ψ around z. This allows to tune each parameter of the tensor $\overline{\overline{B}}$. Following the guidelines presented in section III, the characteristics of both surfaces to obtain left-handed circular polarisation (LHCP) are:

$$\overline{\overline{T}}(k_\rho, 0) = \begin{bmatrix} j200 & 0 \\ 0 & -j13000 \end{bmatrix},$$

$$\overline{\overline{B}}_{LHCP}(k_\rho, 0) = \begin{bmatrix} j950 & j500 \\ j500 & j420 \end{bmatrix}. \qquad (15)$$

$\overline{\overline{T}}$ can be obtained by using a full-wave simulator considering a unit-cell scenario with Floquet boundary conditions. The case of $\overline{\overline{B}}_{LHCP}$ is more complicated to address, since it is not straightforward to tune independently the three desired values of the matrix. Therefore, by considering (21) and (22) in Appendix A, it is possible to reduce the problem to the synthesis of only two components of the tensor and finding the angle $\phi = 59°$ where the diagonal components are zero [37].

$$\overline{\overline{B}}_{LHCP}((k_\rho, 59°) = $$
$$\begin{bmatrix} R^{-1}(59°) \end{bmatrix} \begin{bmatrix} j950 & j500 \\ j500 & j420 \end{bmatrix} \begin{bmatrix} R(59°) \end{bmatrix} \qquad (16)$$
$$= \begin{bmatrix} j1250 & 0 \\ 0 & j119 \end{bmatrix},$$

where $\begin{bmatrix} R(\phi) \end{bmatrix}$ is defined in (23). The angle found to diagonalized the matrix corresponds to the angle of rotation ψ of the HIS. As for the synthesis of the PRS, using the full-wave solver HFSS, the HIS is easily synthesized. Similarly as in (14), the variation of the phase of $\Gamma_{11}^{\overline{\overline{B}}}(\theta, 59°)$ and $\Gamma_{22}^{\overline{\overline{B}}}(\theta, 59°)$ are derived and presented in Fig. 9. Both phase vary less than 5% in the considered frequency band and angles of incidence, which valid the assumptions made in this work. As a result, over the frequency band on interest (12-16GHz) and for a limited scanning angle ($\pm 25°$), the assumptions made for both impedances are valid.
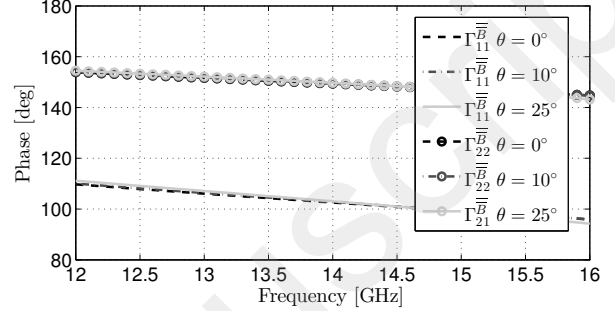

Fig. 9. Phase of the reflection coefficient of the adapted PRS.

B. Circular Polarization Orientation

As presented in Section III.C, the HIS of the form (16) leads to LHCP. It might be of interest to realize right-handed CP (RHCP), and this can be easily done by changing the signs of B_{12} and B_{21} in (15) as

$$\overline{\overline{B}}_{RHCP}(k_\rho, 0) = \begin{bmatrix} j950 & -j500 \\ -j500 & j420 \end{bmatrix}. \qquad (17)$$

Following the same procedure, $\overline{\overline{B}}_{RHCP}$ may be diagonalized as

$$\overline{\overline{B}}_{RHCP}(k_\rho, -59°) = $$
$$\begin{bmatrix} R^{-1}(-59°) \end{bmatrix} \begin{bmatrix} j950 & -j500 \\ -j500 & j420 \end{bmatrix} \begin{bmatrix} R(-59°) \end{bmatrix} \qquad (18)$$
$$= \begin{bmatrix} j1250 & 0 \\ 0 & j119 \end{bmatrix},$$

which leads to the same parameters as in (16). Consequently, RHCP or LHCP may be chosen by considering respectively a rotation $+\psi$ or $-\psi$ of the HIS.

C. Simulation Results

To avoid spurious radiation at the edge of the antenna, the antenna is dimensioned so that the field level reaching its edges is at least 15 dB lower than the level at the center. Following [25], this corresponds to a radiation efficiency of the HLW of about 98%. The antenna is extended of 2λ around the source. Therefore, the $5\lambda \times 5\lambda \times 1\lambda$ full structure is simulated using the full-wave solver HFSS.

As presented in Fig. 8, two slots are etched on the ground plane for matching purpose. The couple of slots in the ground plane are fed by a waveguide transition that have been designed by full-wave simulations. The waveguide transition is
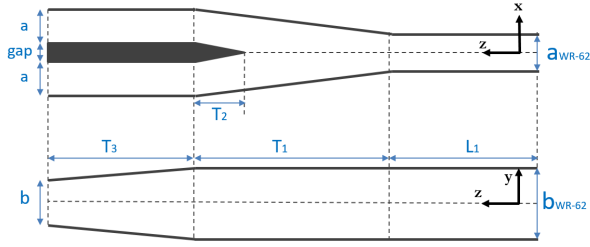
Fig. 10. Right (top) and front (bottom) view of the waveguide power divider. The dimensions are $a = 8$ mm, $b = 12$ mm, $gap = 2$ mm, $L_1 = 10$ mm, $T_1 = 20$ mm, $T_2 = 7$ mm, and $T_3 = 10$ mm.
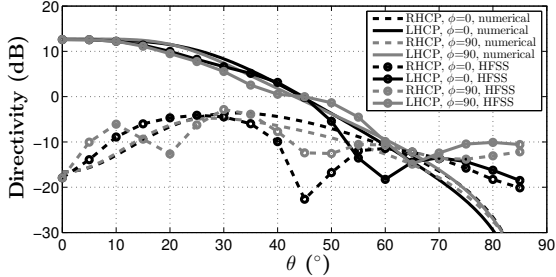

Fig. 11. Normalized radiation pattern at 14.6 GHz for two cut planes. Source size: a=8 mm, b=12mm, gap=2 mm.
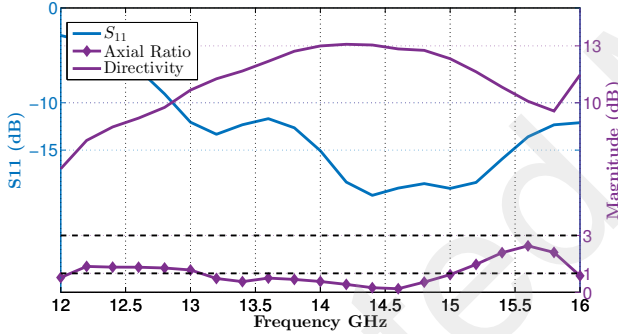

Fig. 12. Simulated performance of the synthesized antenna. Ohmic, dielectric and return loss are considered in the simulations. The strip grids are made of brass with thickness 0.1mm. The spacers are made of HF51 foam ($\epsilon_r = 1.067$ and $tan(\delta_d) = 0.0041$ at 10 GHz).

depicted in Fig. 10 along with its dimensions. A comparison between full-wave simulations and the proposed tool is provided in Fig. 11; good agreement is observed. Fig. 12 presents the performance of the antenna in terms of directivity, AR and matching around the central frequency $f_0 = 14$ GHz. The antenna is matched and presents a directivity variation smaller than 3 dB in the band 12.8-16 GHz (22.9%). Besides, the AR is lower than 3 dB in the band 12-16 GHz (28.5%). In Table II, a comparison between the work presented here and some contributions in the literature is proposed, for similar directivity peak values. For example, in [20], [23], [24], [36] LP primary sources slanted by 45 ° are utilized to feed the cavity. As detailed in section II, two LW modes need to be excited in the cavity to generate CP. In the work presented here, a single HLW is excited allowing a wide AR bandwidth, suitable for small aperture sources for a wide gain-bandwidth

product.

VI. CONCLUSION

A circularly-polarized Fabry-Perot antenna based on a hybrid LW mode has been presented in this paper. Based on a spectral Green's function approach and the definition of a tensorial equivalent model, the antenna has been analyzed from a LW perspective. Resorting to a residue analysis, it has been showed that a single leaky mode is sufficient to produce CP in a wide band. Several assumptions have been made to derive the theoretical formulation. In particular, we have assumed that the PRS and HIS tensor impedances do not change with the frequency and angle of incidence around broadside. In spite of these approximations, the proposed tool becomes very useful to find a first theoretical design. A full-wave analysis is then necessary to synthesize realistic PRS and HIS structures. The simulated results agree with the numerical results of the proposed tool, thus validating the approach and main conclusions. A design example is also proposed validating the approach. The proposed antenna shows a wide band operation, 21.5% around 14 GHz, which is a significant improvement, of about 8%, with respect to the literature. The proposed antenna is within the state of the art in terms of compactness. No dielectric materials are needed to manufacture the antenna, which is very appealing for space applications.

APPENDIX

A. Definition of the tensor impedances

The impedances $\overline{\overline{T}}$ and $\overline{\overline{B}}$ are represented by the following tensors

$$\overline{\overline{T}}(k_\rho, \Omega) = \begin{bmatrix} T_{11}(k_\rho, \Omega) & T_{12}(k_\rho, \Omega) \\ T_{21}(k_\rho, \Omega) & T_{22}(k_\rho, \Omega) \end{bmatrix}, \quad (19)$$

$$\overline{\overline{B}}(k_\rho, \Omega) = \begin{bmatrix} B_{11}(k_\rho, \Omega) & B_{12}(k_\rho, \Omega) \\ B_{21}(k_\rho, \Omega) & B_{22}(k_\rho, \Omega) \end{bmatrix}. \quad (20)$$

Considering a reference value in the plane $\Omega = \phi = 0$ (see Fig. 1) and normal incidence, the impedances in (19), (20) can be written as

$$\overline{\overline{T}}(k_\rho, \Omega) = \begin{bmatrix} R^{-1}(\Omega) \end{bmatrix} \begin{bmatrix} T_{11}(0) & T_{12}(0) \\ T_{21}(0) & T_{22}(0) \end{bmatrix} \begin{bmatrix} R(\Omega) \end{bmatrix}, \quad (21)$$

$$\overline{\overline{B}}(k_\rho, \Omega) = \begin{bmatrix} R^{-1}(\Omega) \end{bmatrix} \begin{bmatrix} B_{11}(0) & B_{12}(0) \\ B_{21}(0) & B_{22}(0) \end{bmatrix} \begin{bmatrix} R(\Omega) \end{bmatrix}, \quad (22)$$

where [37], [39]

$$\begin{bmatrix} R(\Omega) \end{bmatrix} = \begin{bmatrix} \cos(\Omega) & -\sin(\Omega) \\ \sin(\Omega) & \cos(\Omega) \end{bmatrix}. \quad (23)$$

$T_{11}(0)$, $B_{11}(0)$ are the impedances seen by the x-polarized waves, $T_{22}(0)$, $B_{22}(0)$ are the ones affecting the y-polarized ones, and $T_{12}(0)$, $T_{21}(0)$, $B_{12}(0)$, $B_{21}(0)$ account for the coupling between both polarizations. Considering reciprocity [40], [41] $T_{12}(0) = T_{21}(0)$ and $B_{12}(0) = B_{21}(0)$. This synthesis method allows to obtain the tensor impedances at any desired Ω value from a given reference.

B. Analytic derivation of the currents and voltages

The calculations to compute the voltages v_{TE} and v_{TM} in Fig. 2 are presented for the case for which the TM line is fed and the TE line is ended by a short-circuit. The calculations for TE line fed and TM line closed on a short-circuit are very similar, and hence not presented in this appendix. The superscript TM on the current and voltages indicates that a voltage source is placed in the TM line and the one in the TE line is short-circuited. Rigorously, due to the anisotropy of the PRS and the HIS, all the currents and voltages depend on (k_ρ, Ω). However, for readability purpose, this dependence is omitted in the derivations. The equivalent transmission line network presented in Fig. 2 can be solved as a ABCD matrix network as presented in Fig. 13(c). All the defined voltages and currents are presented in Fig. 13. Considering the definition of tensors in (19), (20), and the direction of the voltages i_1^{TM} and i_2^{TM} in Fig. 13(c), the following expressions hold

$$
\begin{bmatrix} v_1^{TM} \\ v_2^{TM} \end{bmatrix} = \overline{\overline{B}} \begin{bmatrix} i_1^{TM} \\ -i_2^{TM} \end{bmatrix},
$$
$$
\begin{bmatrix} v_3^{TM} \\ v_4^{TM} \end{bmatrix} = \overline{\overline{T}} \begin{bmatrix} i_3^{TM} \\ i_4^{TM} \end{bmatrix}. \tag{24}
$$

And therefore, it can be defined $\overline{\overline{B}}_{ABDC}$, and $\overline{\overline{T}}_{ABDC}$ as

$$
\overline{\overline{B}}_{ABDC} = \begin{bmatrix} B_{11}/B_{21} & \frac{B_{11}B_{22}-B_{12}B_{21}}{B_{21}} \\ 1/B_{21} & B_{22}/B_{21} \end{bmatrix},
$$
$$
\overline{\overline{T}}_{ABDC} = \begin{bmatrix} T_{11}/B_{21} & \frac{T_{12}T_{21}-T_{11}T_{22}}{T_{21}} \\ 1/T_{21} & -T_{22}/B_{21} \end{bmatrix}, \tag{25}
$$

so that

$$
\begin{bmatrix} v_1^{TM} \\ i_1^{TM} \end{bmatrix} = \overline{\overline{B}}_{ABDC} \begin{bmatrix} v_2^{TM} \\ i_2^{TM} \end{bmatrix},
$$
$$
\begin{bmatrix} v_3^{TM} \\ i_3^{TM} \end{bmatrix} = \overline{\overline{T}}_{ABDC} \begin{bmatrix} v_4^{TM} \\ i_4^{TM} \end{bmatrix}. \tag{26}
$$

Now, $\overline{\overline{R}}$ and $\overline{\overline{L}}$ are defined as

$$
\overline{\overline{R}} = \left[\overline{\overline{A}}_{L2}^{TM} \right] \left[\overline{\overline{A}}_{Z0}^{TM} \right],
$$
$$
\overline{\overline{L}} = \left[\overline{\overline{A}}_{SC}^{TE} \right] \left[\overline{\overline{A}}_{L2}^{TE} \right] \left[\overline{\overline{A}}_{Z0}^{TE} \right], \tag{27}
$$

so that

$$
\begin{bmatrix} v_1^{TM} \\ i_{IN}^{TM} - i_1^{TM} \end{bmatrix} = \overline{\overline{R}} \begin{bmatrix} v_3^{TM} \\ i_3^{TM} \end{bmatrix},
$$
$$
\begin{bmatrix} v_2^{TM} \\ i_2^{TM} \end{bmatrix} = \overline{\overline{L}} \begin{bmatrix} v_4^{TM} \\ i_4^{TM} \end{bmatrix}, \tag{28}
$$

where

$$
\overline{\overline{A}}_{L1}^{TM/TE} = \begin{bmatrix} \cos(k_{z1}h) & jZ_1^{TM/TE}\sin(k_{z1}h) \\ j\frac{\sin(k_{z1}h)}{Z_1^{TM/TE}} & \cos(k_{z1}h) \end{bmatrix},
$$
$$
\overline{\overline{A}}_{L2}^{TM/TE} = \begin{bmatrix} \cos(k_{z0}D) & jZ_0^{TM/TE}\sin(k_{z0}D) \\ j\frac{\sin(k_{z0}D)}{Z_0^{TM/TE}} & \cos(k_{z0}D) \end{bmatrix},
$$
$$
\overline{\overline{A}}_{Z0}^{TM/TE} = \begin{bmatrix} 1 & 0 \\ \frac{1}{Z_0^{TM/TE}} & \cos(k_{z0}D) \end{bmatrix}, \tag{29}
$$
$$
\overline{\overline{A}}_{SC}^{TM/TE} = \begin{bmatrix} 1 & 0 \\ \frac{-j}{Z_1^{TM/TE}\tan(k_{z1}h)} & \cos k_{z0}D \end{bmatrix}.
$$

Finally, solving the ABCD matrix network in Fig. 13(c), one can define $\overline{\overline{\Delta}}$ and $\overline{\overline{\Lambda}}$ as

$$
\overline{\overline{\Delta}} = \begin{bmatrix} \Delta_{11} & \Delta_{12} \\ \Delta_{21} & \Delta_{22} \end{bmatrix} = \overline{\overline{B}}_{ABDC}\overline{\overline{L}},
$$
$$
\overline{\overline{\Lambda}} = \begin{bmatrix} \Lambda_{11} & \Lambda_{12} \\ \Lambda_{21} & \Lambda_{22} \end{bmatrix} = \overline{\overline{R}}\,\overline{\overline{T}}_{ABDC}, \tag{30}
$$

so that

$$
\begin{bmatrix} v_1^{TM} \\ i_1^{TM} \end{bmatrix} = \overline{\overline{\Delta}} \begin{bmatrix} v_4^{TM} \\ i_4^{TM} \end{bmatrix},
$$
$$
\begin{bmatrix} v_1^{TM} \\ i_{IN}^{TM} - i_1^{TM} \end{bmatrix} = \overline{\overline{\Lambda}} \begin{bmatrix} v_4^{TM} \\ i_4^{TM} \end{bmatrix}. \tag{31}
$$

And finally a system of four equations can be defined as follows

$$
\Lambda_{11}v_4^{TM} + \Lambda_{12}i_4^{TM} = \frac{1 - jZ_1^{TM}\sin(k_{z1}h)i_{IN}^{TM}}{\cos(k_{z1}h)} \tag{32}
$$

$$
\Lambda_{21}v_4^{TM} + \Lambda_{22}i_4^{TM} = i_{IN}^{TM} - i_1^{TM} \tag{33}
$$

$$
\Delta_{11}v_4^{TM} + \Delta_{12}i_4^{TM} = \frac{1 - jZ_1^{TM}\sin(k_{z1}h)i_{IN}^{TM}}{\cos(k_{z1}h)} \tag{34}
$$

$$
\Delta_{21}v_4^{TM} + \Delta_{22}i_4^{TM} = i_1^{TM} \tag{35}
$$

From (32) and (34)

$$
v_4^{TM} = \frac{\Delta_{12} - \Lambda_{12}}{\Lambda_{11} - \Delta_{11}}i_4^{TM}. \tag{36}
$$

From (33) and (35)

$$
i_{IN}^{TM} = v_4^{TM}\left(\Lambda_{21} + \Delta_{21}\right) + i_4^{TM}\left(\Lambda_{22} + \Delta_{22}\right). \tag{37}
$$

Therefore, using the expression of v_4^{TM} in (36), we define K_{IN}^{TM} as

$$
K_{IN}^{TM} = \frac{\left(\Lambda_{21} + \Delta_{21}\right)\left(\Delta_{12} - \Lambda_{12}\right)}{\Lambda_{11} - \Delta_{11}} + \Lambda_{22} + \Delta_{22} \tag{38}
$$

such as

$$
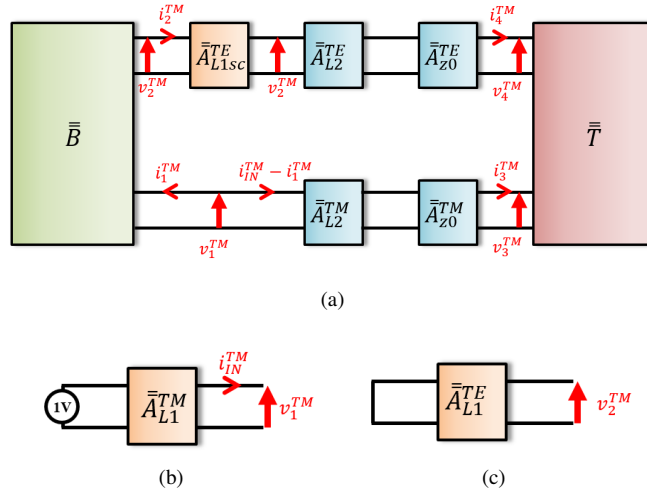i_{IN}^{TM} = K_{IN}^{TM}i_4^{TM}, \tag{39}
$$

Fig. 13. (a) ABCD matrix representation of the FPA where (b) the TM line is fed and (c) the TE line is closed on a short-circuit. The superscript TM on the currents and voltages indicates that a voltage source is placed in the TM line and the one in the TE line is short-circuited.

and in (32) by replacing v_4^{TM} and i_{IN}^{TM} by the expressions in (36) and (39) it follows that

$$i_4^{TM} = \frac{K_{i4}^{-1}}{\cos(k_{z1}h)}, \tag{40}$$

where

$$K_{i4} = \frac{\Lambda_{11}\left(\Delta_{12} - \Lambda_{12}\right)}{\left(\Lambda_{11} - \Delta_{11}\right)} + \Lambda_{12} + jZ_1^{TM}\tan(k_{z1}h)K_{IN}^{TM}. \tag{41}$$

Now that i_4^{TM} is known, v_4^{TM} shall be solved by using (36) and then with (26) v_3^{TM} and i_3^{TM} can be calculated.

C. Spectral GF derivation

Since the GF is sampled with respect to the observation plane ϕ, the use of polar coordinates is more suitable. The spectral dyadic GF of layered media associated with a horizontal magnetic source is sampled with respect to the observation plane ϕ. By linear superposition, the GF used in (2) is defined as

$$\tilde{\boldsymbol{G}}_t^{EM}(k_\rho, \Omega, v_{TE}, v_{TM}) = \begin{bmatrix} v_3^{TEfeed}(k_\rho, \Omega) & v_3^{TMfeed}(k_\rho, \Omega) \\ v_4^{TEfeed}(k_\rho, \Omega) & v_4^{TMfeed}(k_\rho, \Omega) \end{bmatrix} \tag{42}$$

ACKNOWLEDGEMENT

REFERENCES

[1] G. V. Trentini, "Partially reflecting sheet arrays," *IRE Transactions on Antennas and Propagation*, vol. 4, no. 4, pp. 666–671, October 1956.

[2] A. P. Feresidis and J. C. Vardaxoglou, "High gain planar antenna using optimised partially reflective surfaces," *IEE Proceedings - Microwaves, Antennas and Propagation*, vol. 148, no. 6, pp. 345–350, Dec 2001.

[3] D. Blanco, E. Rajo-Iglesias, S. Maci, and N. Llombart, "Directivity enhancement and spurious radiation suppression in leaky-wave antennas using inductive grid metasurfaces," *IEEE Transactions on Antennas and Propagation*, vol. 63, no. 3, pp. 891–900, March 2015.

[4] M. U. Afzal and K. P. Esselle, "Steering the beam of medium-to-high gain antennas using near-field phase transformation," *IEEE Transactions on Antennas and Propagation*, vol. 65, no. 4, pp. 1680–1690, April 2017.

[5] F. Scattone, M. Ettorre, B. Eddo, R. Sauleau, and N. J. G. Fonseca, "Truncated leaky-wave antenna with cosecant-squared radiation pattern," *IEEE Antennas and Wireless Propagation Letters*, vol. 17, no. 5, pp. 841–844, May 2018.

[6] B. B. Tierney and A. Grbic, "Arbitrary beam shaping using 1-D impedance surfaces supporting leaky waves," *IEEE Transactions on Antennas and Propagation*, vol. 63, no. 6, pp. 2439–2448, June 2015.

[7] R. Sauleau, P. Coquet, T. Matsui, and J. . Daniel, "A new concept of focusing antennas using plane-parallel Fabry-Perot cavities with nonuniform mirrors," *IEEE Transactions on Antennas and Propagation*, vol. 51, no. 11, pp. 3171–3175, Nov 2003.

[8] Y. Zheng, J. Gao, Y. Zhou, X. Cao, H. Yang, S. Li, and T. Li, "Wideband gain enhancement and RCS reduction of Fabry-Perot resonator antenna with chessboard arranged metamaterial superstrate," *IEEE Transactions on Antennas and Propagation*, vol. 66, no. 2, pp. 590–599, Feb 2018.

[9] M. Garcia-Vigueras, J. L. Gomez-Tornero, G. Goussetis, A. R. Weily, and Y. J. Guo, "Efficient synthesis of 1-D Fabry-Perot antennas with low sidelobe levels," *IEEE Antennas and Wireless Propagation Letters*, vol. 11, pp. 869–872, 2012.

[10] A. P. Feresidis, G. Goussetis, S. Wang, and J. C. Vardaxoglou, "Artificial magnetic conductor surfaces and their application to low-profile high-gain planar antennas," *IEEE Transactions on Antennas and Propagation*, vol. 53, no. 1, pp. 209–215, Jan 2005.

[11] A. Ourir, A. de Lustrac, and J.-M. Lourtioz, "All-metamaterial-based subwavelength cavities for ultrathin directive antennas," *Applied Physics Letters*, vol. 88, no. 8, p. 084103, 2006.

[12] D. R. Jackson, P. Burghignoli, G. Lovat, F. Capolino, J. Chen, D. R. Wilton, and A. A. Oliner, "The fundamental physics of directive beaming at microwave and optical frequencies and the role of leaky waves," *Proceedings of the IEEE*, vol. 99, no. 10, pp. 1780–1805, Oct 2011.

[13] M. Garcia-Vigueras, J. L. Gomez-Tornero, G. Goussetis, A. R. Weily, and Y. J. Guo, "Enhancing frequency-scanning response of leaky-wave antennas using high-impedance surfaces," *IEEE Antennas and Wireless Propagation Letters*, vol. 10, pp. 7–10, 2011.

[14] F. Qin, S. Gao, G. Wei, Q. Luo, C. Mao, C. Gu, J. Xu, and J. Li, "Wideband circularly polarized Fabry-Perot antenna," *IEEE Antennas and Propagation Magazine*, vol. 57, no. 5, pp. 127–135, Oct 2015.

[15] B. A. Zeb, N. Nikolic, and K. P. Esselle, "A high-gain dual-band EBG resonator antenna with circular polarization," *IEEE Antennas and Wireless Propagation Letters*, vol. 14, pp. 108–111, 2015.

[16] A. R. Weily, K. P. Esselle, T. S. Bird, and B. C. Sanders, "High gain circularly polarised 1-D EBG resonator antenna," *Electronics Letters*, vol. 42, no. 18, pp. 1012–1013, Aug 2006.

[17] R. K. M. Lou and M. Naser-Moghadasi, "Wideband aperture-coupled antenna array based on Fabry-Perot resonator for C-band applications," *IET Microwaves, Antennas Propagation*, vol. 11, no. 6, pp. 859–866, 2017.

[18] D. Comite, P. Baccarelli, P. Burghignoli, and A. Galli, "Omnidirectional 2-D leaky-wave antennas with reconfigurable polarization," *IEEE Antennas and Wireless Propagation Letters*, vol. 16, pp. 2354–2357, 2017.

[19] M. Diblanc, E. Rodes, E. Arnaud, M. Thevenot, T. Monediere, and B. Jecko, "Circularly polarized metallic EBG antenna," *IEEE Microwave and Wireless Components Letters*, vol. 15, no. 10, pp. 638–640, Oct 2005.

[20] S. A. Muhammad, R. Sauleau, L. L. Coq, and H. Legay, "Self-generation of circular polarization using compact Fabry-Perot cavity antennas," *IEEE Antennas and Wireless Propagation Letters*, vol. 10, pp. 907–910, 2011.

[21] S. A. Muhammad, R. Sauleau, and H. Legay, "Purely metallic waveguide-fed Fabry-Perot cavity antenna with a polarizing frequency selective surface for compact solutions in circular polarization," *IEEE Antennas and Wireless Propagation Letters*, vol. 11, pp. 881–884, 2012.

[22] R. Orr, G. Goussetis, and V. Fusco, "Design method for circularly polarized Fabry-Perot cavity antennas," *IEEE Transactions on Antennas and Propagation*, vol. 62, no. 1, pp. 19–26, Jan 2014.

[23] Z. G. Liu, Z. X. Cao, and L. N. Wu, "Compact low-profile circularly polarized Fabry-Perot resonator antenna fed by linearly polarized microstrip patch," *IEEE Antennas and Wireless Propagation Letters*, vol. 15, pp. 524–527, 2016.

[24] J. Ren, W. Jiang, K. Zhang, and S. Gong, "A high-gain circularly polarized Fabry-Perot antenna with wideband low-RCS property," *IEEE Antennas and Wireless Propagation Letters*, vol. 17, no. 5, pp. 853–856, May 2018.

[25] J. Volakis, A. A. Olliner, and D. R. Jackson, *Antenna Engineering Handbook*. US: McGraw-Hill, 2007, ch. 7, Leaky Wave Antennas.

[26] S. A. Muhammad, R. Sauleau, G. Valerio, L. L. Coq, and H. Legay, "Self-polarizing Fabry-Perot antennas based on polarization twisting element," *IEEE Transactions on Antennas and Propagation*, vol. 61, no. 3, pp. 1032–1040, March 2013.

[27] M. Garcia-Vigueras, J. L. Gomez-Tornero, G. Goussetis, A. R. Weily, and Y. J. Guo, "1D-leaky wave antenna employing parallel-plate waveguide loaded with PRS and HIS," *IEEE Transactions on Antennas and Propagation*, vol. 59, no. 10, pp. 3687–3694, Oct 2011.

[28] C. A. Balanis, *Antenna Theory: Analysis and Design*. Hoboken: John Wiley, 2005.

[29] L. B. Felsen and N. Marcuvitz, *Radiation and Scattering of Waves*. New York: IEEE Press, 1994.

[30] B. D. Bates and G. W. Staines, *Transverse Resonance Analysis Technique for Microwave and Millimetre-Wave Circuits*. Salsbury: DSTO Electronics and Surveillance Research Laboratory, 1995.

[31] R. E. Collin and F. J. Zucker, *Antenna Theory, Part 2*. US: McGraw-Hill, 1969, ch. 19, 20.

[32] A. M. Patel and A. Grbic, "Effective surface impedance of a printed-circuit tensor impedance surface (pctis)," *IEEE Transactions on Microwave Theory and Techniques*, vol. 61, no. 4, pp. 1403–1413, April 2013.

[33] O. Luukkonen, C. Simovski, G. Granet, G. Goussetis, D. Lioubtchenko, A. V. Raisanen, and S. A. Tretyakov, "Simple and accurate analytical model of planar grids and high-impedance surfaces comprising metal strips or patches," *IEEE Transactions on Antennas and Propagation*, vol. 56, no. 6, pp. 1624–1632, June 2008.

[34] V. Torres, F. Mesa, M. Navarro-Cia, R. Rodriguez-Berral, M. Beruete, and F. Medina, "Accurate circuit modeling of fishnet structures for negative-index-medium applications," *IEEE Transactions on Microwave Theory and Techniques*, vol. 64, no. 1, pp. 15–26, Jan 2016.

[35] A. Neto, N. Llombart, G. Gerini, M. D. Bonnedal, and P. de Maagt, "EBG enhanced feeds for the improvement of the aperture efficiency of reflector antennas," *IEEE Transactions on Antennas and Propagation*, vol. 55, no. 8, pp. 2185–2193, Aug 2007.

[36] K. Li, Y. Liu, Y. Jia, and Y. J. Guo, "A circularly polarized high-gain antenna with low RCS over a wideband using chessboard polarization conversion metasurfaces," *IEEE Transactions on Antennas and Propagation*, vol. 65, no. 8, pp. 4288–4292, Aug 2017.

[37] X. Artiga, D. Bresciani, H. Legay, and J. Perruisseau-Carrier, "Polarimetric control of reflective metasurfaces," *IEEE Antennas and Wireless Propagation Letters*, vol. 11, pp. 1489–1492, 2012.

[38] R. Rodriguez-Berral, C. Molero, F. Medina, and F. Mesa, "Analytical wideband model for strip/slit gratings loaded with dielectric slabs," *IEEE Transactions on Microwave Theory and Techniques*, vol. 60, no. 12, pp. 3908–3918, Dec 2012.

[39] C. Pfeiffer and A. Grbic, "Bianisotropic metasurfaces: Ultra-thin surfaces for complete control of electromagnetic wavefronts," *Physic Review Application*, Apr. 2014.

[40] D. M. Pozar, *Microwave Engineering*. Hoboken: John Wiley, 2012.

[41] H. J. Bilow, "Guided waves on a planar tensor impedance surface," *IEEE Transactions on Antennas and Propagation*, vol. 51, no. 10, pp. 2788–2792, Oct 2003.